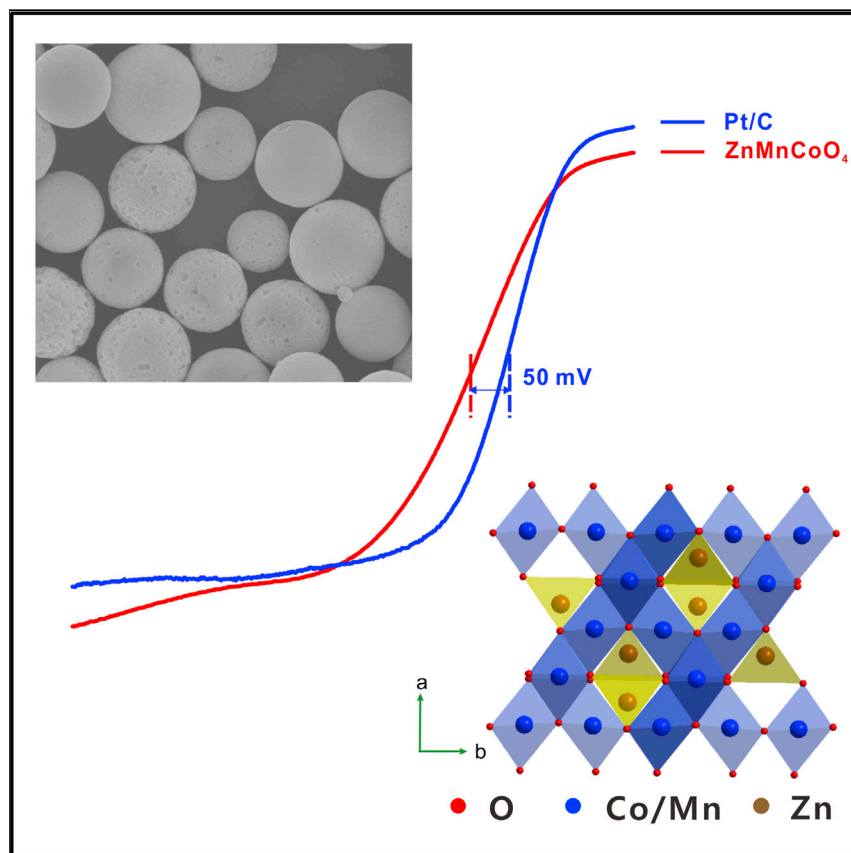


Article

Durable and Efficient Hollow Porous Oxide Spinel Microspheres for Oxygen Reduction



The oxygen reduction reaction performance of the hollow porous oxide spinel microspheres was investigated. The ZnMnCoO_4 possessed a high onset potential of 1.00 V and an outstanding durability in the alkaline solution. The electronic transition of Co^{3+} ions was found to weaken the $\text{Co}^{3+}\text{-OH}$ bond and facilitate the $\text{O}^{2-}/\text{OH}^-$ displacement. Thus, it may offer promising potential for use as an effective catalyst with high oxygen reduction activity and durability in fuel cells and metal-air batteries, among other applications.

Hao Wang, Ruiping Liu, Yutao Li, ..., Ru Zhang, Ming Lei, Zhiqun Lin

lytthu@gmail.com (Y.L.)
mlei@bupt.edu.cn (M.L.)
zhiqun.lin@mse.gatech.edu (Z.L.)

HIGHLIGHTS

We synthesize hollow porous oxide spinel microspheres

The ZnMnCoO_4 microspheres exhibit the best oxygen reduction activity

The ZnMnCoO_4 microspheres show excellent durability in the alkaline solution

The superior performance is ascribed to the electronic transition of Co^{3+} ions

Article

Durable and Efficient Hollow Porous Oxide Spinel Microspheres for Oxygen Reduction

Hao Wang,^{1,2,6} Ruiping Liu,^{3,4,6} Yutao Li,^{2,*} Xujie Lü,⁵ Qi Wang,³ Shiqiang Zhao,⁴ Kunjie Yuan,⁴ Zhiming Cui,² Xiang Li,² Sen Xin,² Ru Zhang,¹ Ming Lei,^{1,*} and Zhiqun Lin^{4,7,*}

HPSTAR
573-2018

SUMMARY

Transition metal oxide catalysts with high oxygen reduction activity and durability are highly desirable for use in fuel cells and metal-air batteries. Herein we report, for the first time, the oxygen reduction activity of hollow porous spinel AB_2O_4 microspheres, where A = Zn^{2+} and B = Mn^{3+} and/or Co^{3+} (i.e., $ZnMn_xCo_{2-x}O_4$). Among them, $ZnMnCoO_4$ ($x = 1$) microspheres exhibit the best oxygen reduction activity with a half-wave-potential only 50 mV lower than that of the Pt/C counterpart and an excellent durability in the alkaline solution. Importantly, the electronic transition of Co^{3+} ions from low-spin state in commercial Co_3O_4 catalyst to a mixed high-spin and low-spin state in $ZnMnCoO_4$ catalyst was found to weaken the Co^{3+} -OH bond and facilitate the O^{2-}/OH^- displacement. The density functional theory calculation substantiated that $ZnMnCoO_4$ displayed a more favorable binding energy with O_2 and oxygenated species, thereby enabling the fast reaction kinetics in the oxygen reduction reaction process.

INTRODUCTION

Due to high cost of noble-metal catalysts and the declining oxygen reduction activity on the cathode of proton exchange membrane (PEM) fuel cells and metal-air batteries, recent research has witnessed intense investigation into the promising and versatile non-precious catalysts for the oxygen reduction reaction (ORR).^{1–5} To this end, several low-cost non-noble-metal alternatives have emerged, including carbon-based materials,^{6–9} non-precious transition metals and metal alloys (e.g., Fe, Co, Ni-Cu alloy),^{10–12} and transition metal oxides (e.g., Fe_3O_4 , Co_3O_4).^{13,14} However, transition metal oxides often possess high overpotentials. Moreover, carbon-based catalysts and transition metal alloys often involve poor durability, thus preventing them from large-scale commercial applications in PEM fuel cells and metal-air batteries.

It is notable that the activity of ORR catalysts is primarily controlled by their electronic structures, where the energy released due to the bond formation of $M^{(m+1)+}-O_2^{2-}$ ($M = Co, Mn$, etc.) on the surface of catalyst is required to be close enough to the energy needed to break the $M^{m+}-OH^-$ ($M = Co, Mn$, etc.) bond to ensure a fast displacement of O^{2-}/OH^- and OH^- regeneration.¹⁵ As an important class of metal oxides, perovskite oxides (ABO_3) with the σ^* antibonding orbital ($e_g = 1$) displays the highest ORR activity.¹⁶ However, most perovskite oxides tend to dissolve in an acid solution and their surface amorphization usually occurs in an alkaline solution.¹⁷ Notably, Co^{3+} -based oxides such as Co_3O_4 and $LaCoO_3$ have been explored as promising ORR catalysts.^{18,19} The reasons are twofold. First, the $Co^{3+}-O^{2-}$ and $Co^{3+}-OH$ possess the moderate bond strength. Second, Co^{3+} with

Context & Scale

Transition metal oxide catalysts with high oxygen reduction activity and durability are highly desirable as they promise new opportunities as alternatives to rare noble-metal catalysts for use in fuel cells and metal-air batteries. However, transition metal oxides often possess high overpotentials. In this paper, we report the crafting of a family of Co^{3+} -based spinel oxides (AB_2O_4 : A = Zn^{2+} and B = Mn^{3+} and/or Co^{3+}) and the subsequent exploration of their use as catalysts in the oxygen reduction reaction (ORR) by scrutinizing the correlation between the electronic structure of Co^{3+} ions and the resulting ORR performance. Among them, $ZnMnCoO_4$ ($x = 1$) microspheres where Mn and Co ions are located at the B site of spinel AB_2O_4 were found to exhibit the best oxygen reduction activity, with a half-wave-potential only 50 mV lower than that of the Pt/C counterpart and an excellent durability in the alkaline solution. The electronic transition of Co^{3+} ions from low-spin state in commercial Co_3O_4 catalyst to a mixed high-spin and low-spin state in $ZnMnCoO_4$ catalyst was found to weaken the $Co^{3+}-OH$ bond and facilitate the O^{2-}/OH^- displacement.



six $3d$ electrons is on the border of high-spin states ($t_{2g}^4 e_g^2$) and low-spin states ($t_{2g}^6 e_g^0$) owing to their similar crystal field splitting energy (Δ) and the pairing energy (P), making Co^{3+} -based oxides unique as ORR catalysts. The electronic structure of Co^{3+} in oxides depends sensitively on the $\text{Co}^{3+}\text{-O}^{2-}$ bond strength. For example, the electrons in LaCoO_3 undergo a spin-state transition from low-spin states to intermediate-spin states and eventually to high-spin states as temperature increases from 50 to 600 K as a result of the change of the $\text{Co}^{3+}\text{-O}^{2-}$ bond length.²⁰

Herein, we report the crafting of a family of Co^{3+} -based spinel oxides AB_2O_4 ($A = \text{Zn}^{2+}$ and $B = \text{Mn}^{3+}$ and/or Co^{3+}) and the subsequent exploration of their use as catalysts in ORR by scrutinizing the correlation between the electronic structure of Co^{3+} ions and the resulting ORR performance. Moreover, the morphology of materials has a great impact on their catalytic activities. A desirable structure as electrocatalysts should have the abundant active sites and the excellent mass transport ability with the electrolyte. The catalysts with hollow porous structure possessing high surface area and good contact with electrolyte usually show the improved ORR activities. Organic soft template, polyvinyl pyrrolidone (PVP), is often used in forming well-defined porous structure as it can be removed easily by calcination in air after the target structure is obtained. The decomposition of PVP creates the hollow structure, and the release of CO_2 and H_2O results in the porous surface. In this study, the hollow porous $\text{ZnMn}_x\text{Co}_{2-x}\text{O}_4$ ($0 \leq x \leq 2$) microspheres were yielded via a simple two-step process, that is, the synthesis of the coordination complex as precursors containing Zn, Co, and Mn ions, followed by its calcination in air. Compared with solid commercial Co_3O_4 used as control, these $\text{ZnMn}_x\text{Co}_{2-x}\text{O}_4$ microspheres have higher surface areas and more active sites for ORR. Among various spinel oxides $\text{ZnMn}_x\text{Co}_{2-x}\text{O}_4$ crafted, hollow porous ZnMnCoO_4 microspheres exhibited the highest oxygen reduction performance with a half-wave potential 50 mV lower than that of widely used Pt/C and an excellent durability in an alkaline solution. It was found that the stronger $\text{Zn}^{2+}\text{-O}$ bond than $\text{Co}^{2+}\text{-O}$ in the tetrahedral a sites and the larger size of Mn^{3+} ions than Co^{3+} ions in octahedral b sites weakened the $\text{Co}^{3+}\text{-O}$ bond and altered the spin states of Co^{3+} ions, thereby leading to a greatly improved ORR performance of ZnMnCoO_4 compared with that of solid Co_3O_4 and hollow porous ZnCo_2O_4 . More importantly, the density functional theory (DFT) calculation corroborated that the $\text{Co}^{3+}\text{-O}$ and O-O bond distances were increased with the increased incorporation of Mn^{3+} ions, suggesting the suitable bond strength for fast ORR reactions. Moreover, in stark contrast to ZnMn_2O_4 which has a weak interaction with oxygen and a low ORR activity as a result of the largest Mn-O bond distance, ZnMnCoO_4 demonstrated a more energetically favorable binding with O_2 and oxygenated species, thus resulting in the fast ORR kinetics.

RESULTS

The morphology of as-prepared $\text{ZnMn}_x\text{Co}_{2-x}\text{O}_4$ samples were examined by transmission electron microscopy (TEM) and field-emission scanning electron microscopy (FESEM) as shown in Figures 1, S1, and S2, respectively. The ZnCo_2O_4 and ZnMnCoO_4 samples possessed a microsphere-like structure with an average diameter of approximately 750 nm (Figure S1). A hollow interior of ZnCo_2O_4 and ZnMnCoO_4 microspheres is clearly evident in TEM images (Figure 1), where the shell of ZnCo_2O_4 microspheres is slightly thicker than that of ZnMnCoO_4 microspheres. It is not surprising that the hollow interior resulted from thermal decomposition of poly(vinyl pyrrolidone) (PVP) in the PVP-metal-ion-containing precursors (i.e., a coordination complex formed by the coordination of pyrrolidone groups and metal ions;

¹State Key Laboratory of Information Photonics and Optical Communications & School of Science, Beijing University of Posts and Telecommunications, Beijing 100876, China

²Materials Science and Engineering Program and Texas Materials Institute, The University of Texas at Austin, Austin, TX 78712, USA

³Department of Materials Science and Engineering, China University of Mining & Technology (Beijing), Beijing 100083, China

⁴School of Materials Science and Engineering, Georgia Institute of Technology, Atlanta, GA 30332, USA

⁵Center for High Pressure Science and Technology Advanced Research, Shanghai 201203, China

⁶These authors contributed equally

⁷Lead Contact

*Correspondence: lytthu@gmail.com (Y.L.), mlei@bupt.edu.cn (M.L.), zhiqun.lin@mse.gatech.edu (Z.L.)

<https://doi.org/10.1016/j.joule.2017.11.016>

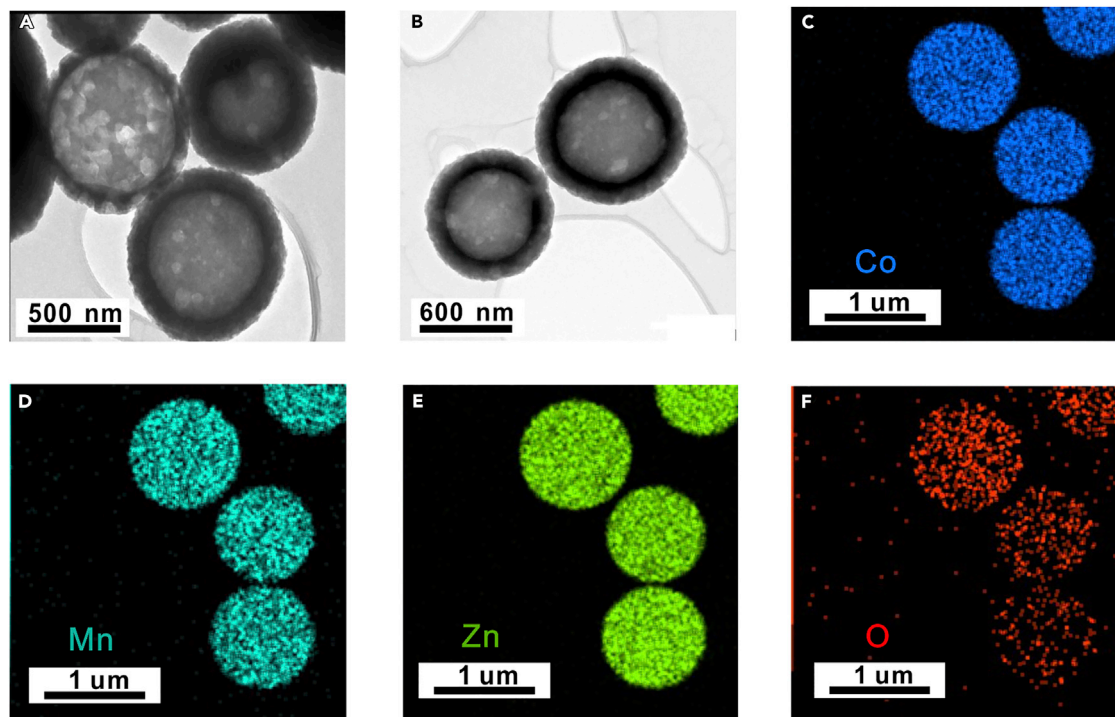


Figure 1. Morphologies and Element Distribution of As-Obtained Microspheres

(A) TEM images of hollow porous ZnCo_2O_4 ($x = 0$). Scale bar, 500 nm.

(B) ZnMnCoO_4 ($x = 1$) microspheres. Scale bar, 600 nm.

(C–F) Elemental mapping of hollow porous ZnMnCoO_4 microspheres: (C) Co, (D) Mn, (E) Zn, and (F) O. Scale bar, 1 μm .

see [Experimental Procedures](#)) in air at high temperature and, moreover, the release of CO_2 created porous surface on microspheres.²¹ The EDX mapping of ZnMnCoO_4 microspheres revealed the uniform distribution of Zn, Mn, Co, and O elements within microsphere ([Figures 1C–1F](#)).

The Brunauer-Emmett-Teller (BET) specific surface area of ZnCo_2O_4 and ZnMnCoO_4 microspheres was found to be 21.2 and 30.9 $\text{m}^2 \text{g}^{-1}$, respectively (see [Experimental Procedures](#)). The pore size distribution was then calculated from the desorption curve of the nitrogen isotherm by the Barrett-Joyner-Halenda method ([Figure S3](#)). The hollow ZnCo_2O_4 microspheres had a pore size over a range of 3.0–16.0 nm with an average pore diameter of approximately 9.7 nm. For ZnMnCoO_4 microspheres, a more uniform pore size distribution with a slightly smaller pore (~ 8.5 nm) was observed.

[Figures 2A](#) and [S4](#) compare the powder X-ray diffraction (XRD) patterns of as-prepared hollow porous $\text{ZnMn}_x\text{Co}_{2-x}\text{O}_4$ microsphere samples and commercially available solid Co_3O_4 powder. A pure phase with cubic spinel structure was obtained for samples with $x = 0$ and 1 (i.e., ZnCo_2O_4 and ZnMnCoO_4). ZnMn_2O_4 with a lattice parameter $a = b = 5.7284 \text{ \AA}$ and $c = 9.1953 \text{ \AA}$ has a tetragonal structure because of the strong Jahn-Teller effect of Mn^{3+} ($t_{2g}^3 e_g^1$). Clearly, tetragonal and cubic phases coexisted in the $\text{ZnMn}_{1.2}\text{Co}_{0.8}\text{O}_4$ sample with $x = 1.2$ ([Figure S4](#)). The diffraction peaks at $2\theta = 18.9^\circ$, 31.2° , 36.8° , 38.4° , 44.7° , 55.5° , 59.2° , and 65.1° correspond to the (111), (220), (311), (222), (400), (422), (511), and (440) lattice planes, respectively. Rietveld analysis of the synchrotron XRD pattern of ZnMnCoO_4 microspheres is shown in [Figure 2B](#) and [Table S1](#) with the reliability

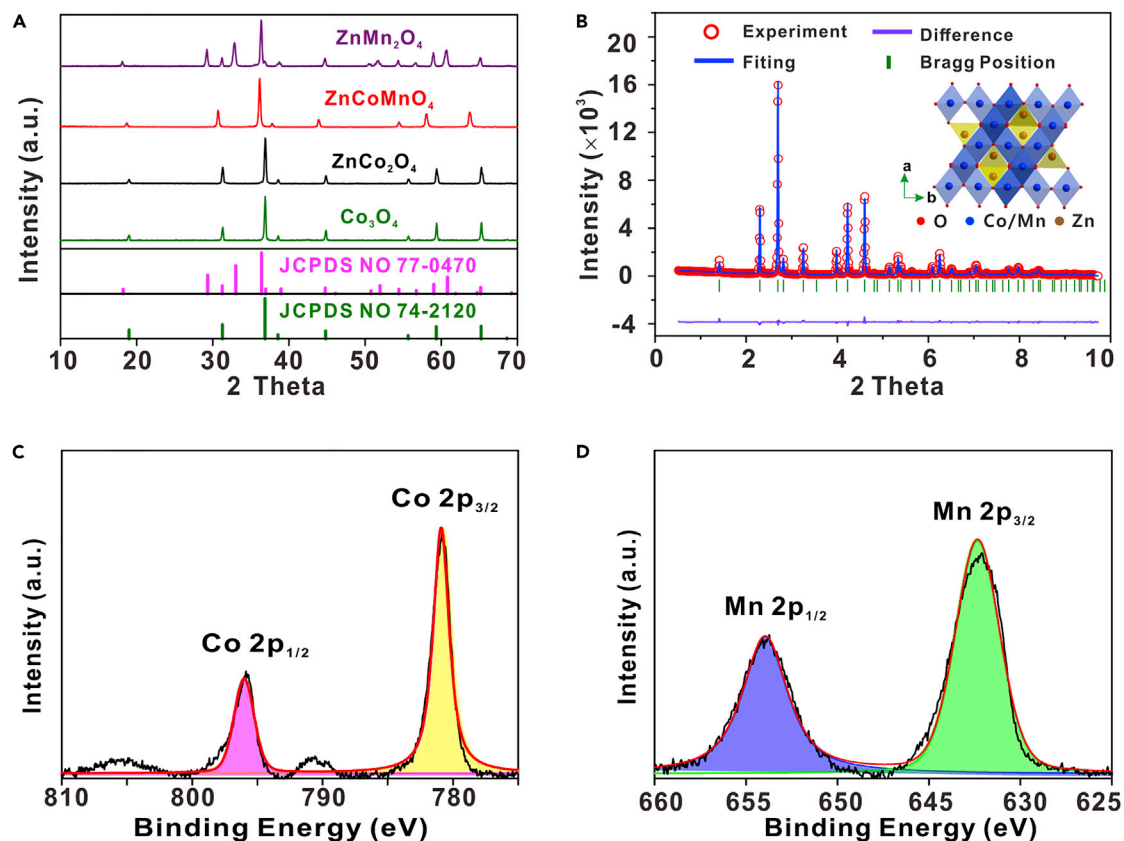


Figure 2. XRD Pattern and XPS of the As-obtained Microspheres

(A) XRD patterns of as-prepared hollow porous ZnMn_xCo_{2-x}O₄ microspheres and commercially available Co₃O₄ powder. The standard XRD profiles of ZnMn₂O₄ (JCPDS no. 77-0470) and Co₃O₄ (JCPDS no. 74-2120) are shown in pink and green, respectively.

(B) Rietveld analysis of the synchrotron XRD of ZnMnCoO₄ (open circles, experimental measurement; red line, fitted profile). The crystal structure of spinel ZnMnCoO₄ is shown as an inset.

(C and D) XPS spectra of (C) Co and (D) Mn in hollow porous ZnMnCoO₄ microspheres.

factors ($R_{wp} = 7.29\%$ and $R_p = 5.26\%$). The cubic spinel phase ZnMnCoO₄ has a space group $Fm\bar{3}m$ with a lattice parameter $a = b = c = 8.2661 \text{ \AA}$. Figures 2C, 2D, and S5 depict the X-ray photoelectron spectroscopy (XPS) results of hollow porous ZnMnCoO₄ microspheres. Clearly, the representative survey XPS spectrum showed the presence of Zn, Mn, Co, and O elements. The two peaks at 1,044.2 eV and 1,021.2 eV can be assigned to Zn 2p_{3/2} and Zn 2p_{1/2} of Zn²⁺ ions, respectively.²² The two peaks at 780.7 eV for Co 2p_{3/2} and 795.8 eV for Co 2p_{1/2}, respectively, are in good agreement with the binding energy of Co³⁺ in pure Co₃O₄. Two Mn 2p_{1/2} and 2p_{3/2} peaks at 653.5 eV and 642.2 eV (Figure 2D) confirmed the existence of Mn³⁺ in ZnMnCoO₄.²³

Figures 3 and S6 compare the ORR performance of as-prepared hollow porous ZnMn_xCo_{2-x}O₄ microspheres, commercial Co₃O₄ powder, and commercial Pt/C powder as catalysts. The ZnMnCoO₄ sample had an onset potential of 1.00 V, nearly the same as that of Pt/C (1.02 V), which is much better than those of the ZnCo₂O₄ sample (0.89 V), Co₃O₄ powder (0.83 V), and the ZnMn₂O₄ sample (0.72 V). Moreover, ZnMnCoO₄ had the highest limiting current density up to 6.2 mA cm⁻² (Figure 3A). The half-wave potential of ZnMnCoO₄ was only 50 mV lower than that of Pt/C and 261 mV higher than that of ZnCo₂O₄ (Figure 3B). Moreover, the ZnMnCoO₄

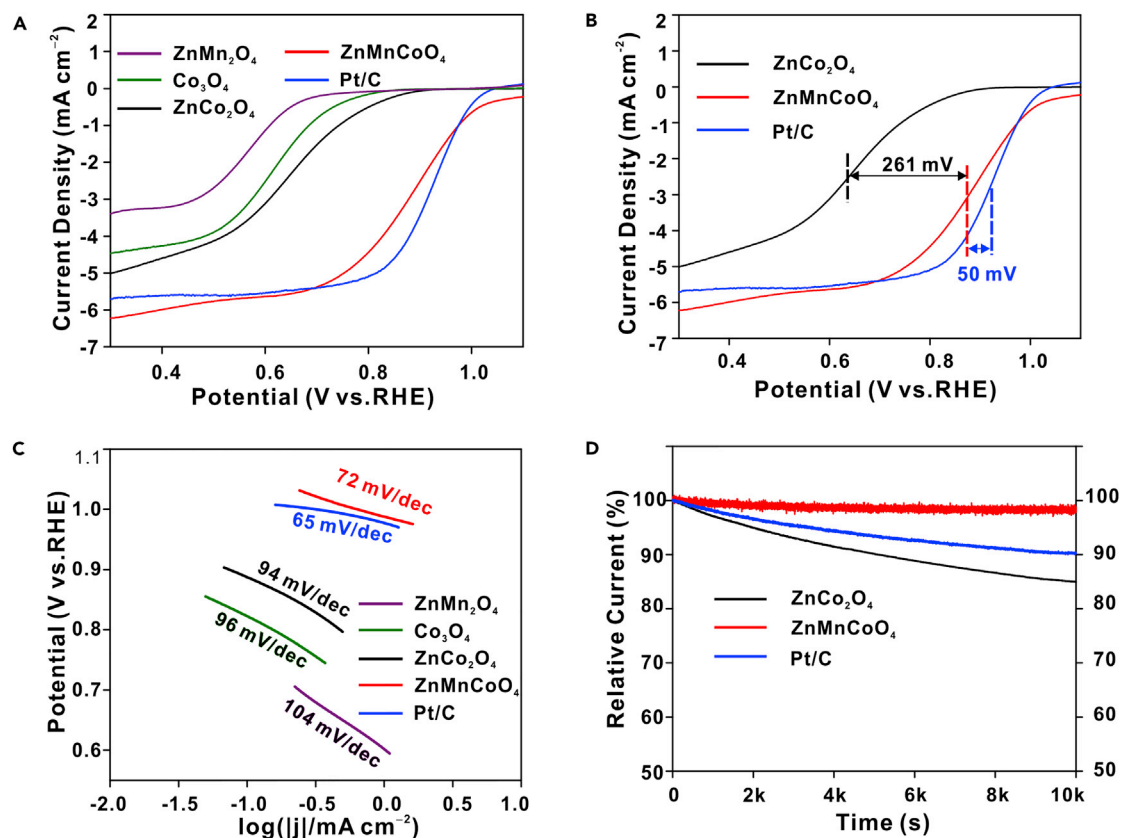


Figure 3. The ORR Performances of the As-Obtained Samples

(A) ORR polarization curves of hollow porous $\text{ZnMn}_x\text{Co}_{2-x}\text{O}_4$ microspheres with different value of x , solid Co_3O_4 powder, and the Pt/C powder as catalysts in an O_2 -saturated 0.1 M KOH solution stirred at 1,600 rpm.

(B) Comparison of the ORR polarization curves among the ZnCo_2O_4 , ZnMnCoO_4 , and Pt/C catalysts in an O_2 -saturated 0.1 M KOH solution stirred at 1,600 rpm.

(C) The Tafel slope of $\text{ZnMn}_x\text{Co}_{2-x}\text{O}_4$, Co_3O_4 powder and Pt/C catalysts.

(D) The chronoamperometric curves of ZnCo_2O_4 and ZnMnCoO_4 catalysts and Pt/C in an O_2 -saturated 0.1 M KOH electrolyte at the fixed voltage of 0.6 V stirred at 1,600 rpm.

sample exhibited a smaller Tafel slope than other spinel oxides (ZnCo_2O_4 and ZnMn_2O_4), signifying its outstanding ORR kinetics (Figures 3C and S6C). The ORR polarization curves and the current densities of $\text{ZnMn}_x\text{Co}_{2-x}\text{O}_4$ with different x at 0.9 V are shown in Figures S6A and S6B, respectively. Clearly, with the increase of Mn^{3+} content, the $\text{ZnMn}_x\text{Co}_{2-x}\text{O}_4$ samples displayed a markedly enhanced ORR performance. Among all hollow porous $\text{ZnMn}_x\text{Co}_{2-x}\text{O}_4$ microsphere catalysts, the ZnMnCoO_4 catalyst demonstrated the highest ORR activity, while the ZnMn_2O_4 catalyst yielded the worst ORR activity with a half-wave potential of 0.56 V. The electrochemical impedance results of $\text{ZnCo}_2\text{O}_4/\text{C}$, $\text{ZnMnCoO}_4/\text{C}$, and $\text{ZnMn}_2\text{O}_4/\text{C}$ are shown in Figure S7. They all have similar charge transfer resistances ($\sim 44 \Omega$), indicating that the electronic structure of the spinel $\text{ZnMn}_x\text{Co}_{2-x}\text{O}_4$ dictates the ORR activity instead of the conductivity.

The durability of the ZnCo_2O_4 , ZnMnCoO_4 , and Pt/C samples at 0.6 V in an O_2 -saturated 0.1 M KOH solution stirred at 1,600 rpm was also investigated (Figure 3D). It is clear that ZnMnCoO_4 possessed better stability than ZnCo_2O_4 and Pt/C. It retained more than 95% of its initial current after 10,000 s, while the ORR currents of Pt/C and ZnCo_2O_4 reached 90% and 86% of their original values, respectively. A 93% of its

original current remains when ZnMnCoO₄ was tested at 0.6 V in O₂-saturated 0.1 M KOH solution for 10 hr (Figure S8), signifying the outstanding stability of ZnMnCoO₄. Moreover, both ZnCo₂O₄ and ZnMnCoO₄ catalysts showed a better methanol tolerance than the commercial Pt/C in a 3 M methanol solution (Figure S6D). Table S2 summarizes the activity and durability of all catalysts studied in this work.

As hollow porous ZnMnCoO₄ microspheres exhibited the highest ORR activity among all ZnMn_xCo_{2-x}O₄ catalysts as noted above, we now turn our attention to further scrutinize the ORR kinetics of ZnMnCoO₄ catalyst in an O₂-saturated 0.1 M KOH. The linear sweep voltammetry (LSV) were measured at different rotation rates and the corresponding Koutecky-Levich (K-L) plots are shown in Figures S9A and S9B. The number of electrons transferred per oxygen molecule calculated from slope of K-L plot was 3.80–3.93, indicating a desirable four-electron ORR pathway. The hydrogen peroxide (H₂O₂) yield and the number of electrons calculated from the disk and ring currents (Figures S9C and S9D) revealed that only approximately 5% HO₂⁻ was produced and the number of electrons transferred was about 3.9, which is consistent with the results from the K-L plot.

DISCUSSION

The interaction between O₂, intermediate species (e.g., *O and *OH) generated during the ORR process, and spinel AB₂O₄ is determined by the electronic structure of the transition metal B ions and the B-O bond character. In spinel AB₂O₄ (A = Zn²⁺ or Co²⁺ and B = Mn³⁺ and/or Co³⁺), Mn³⁺ and Co³⁺ with high crystal field stabilization energy occupy the octahedral 16 b sites and Zn²⁺ and Co²⁺ occupy the tetrahedral 8 a sites to form a typical spinel. Figure S4 shows the lattice parameters increased with the addition of more Mn³⁺ ions in ZnMn_{1-x}Co_xO₄ because of the larger size of Mn³⁺ (0.65 Å) than that of Co³⁺ (0.61 Å for high-spin t_{2g}⁴e_g², and 0.54 Å for low-spin t_{2g}⁶e_g⁰). Co₃O₄ is a paramagnetic semiconductor at room temperature with an antiferromagnetic transition at T_N = 40 K; the high-spin Co²⁺ ions in the tetrahedral sites with 3 unpaired 3d electrons carry a magnetic moment, while the octahedral Co³⁺ ions have a low-spin state with all 3d electrons paired.²⁴ No electron occupied in the σ* antibonding orbital of Co₃O₄ leads to a very strong Co³⁺/O₂ interaction and a quite stable Co⁴⁺-O₂²⁻ bond (step 1 in Figure 4C), making it difficult for the Co⁴⁺-O₂²⁻/Co³⁺-OOH transition (step 2). Moreover, the insufficiently destabilized Co⁴⁺-O₂²⁻ bond also reduces the regeneration rate of *OH (step 4).

The electronic structure of Co³⁺ ions and the Co-O bonding character experiences a change in spinel Co₃O₄ as the Co²⁺ or Co³⁺ ions are replaced by Zn²⁺ or Mn³⁺ ions. The magnetic susceptibility (χ) of hollow ZnCo₂O₄ and ZnMnCoO₄ microspheres is shown in Figures 4A and 4B. ZnMnCoO₄ has an antiferromagnetic-to-paramagnetic transition at 15 K (Figure 4B). In contrast, ZnCo₂O₄ has no such an orbit ordering (i.e., an antiferromagnetic-to-paramagnetic transition) at low temperature (Figure 4A). The non-linear curves from both ZnCo₂O₄ and ZnMnCoO₄ at low temperature in Figures 4A and 4B may be ascribed to the ratio change of high-spin states to low-spin states of Co³⁺ ions, which was induced by the change of Co³⁺-O bond length on the surface of the ZnCo₂O₄ and ZnMnCoO₄ catalysts with temperature. The effective magnetic moments of ZnCo₂O₄ and ZnMnCoO₄ microspheres were calculated to be 3.5 μ_B and 7.9 μ_B per formula, respectively. It is important to note that in ZnCo₂O₄, each Co³⁺ ion was calculated to have a magnetic moment of 2.5 μ_B (Figure 4A), which is close to the intermediate-spin magnetic moment of Co³⁺ ion (t_{2g}⁵e_g¹). According to the XRD measurements noted above (Figures 2A and 2B), the stronger Zn²⁺-O bond within ZnCo₂O₄ than the Co²⁺-O bond within Co₃O₄

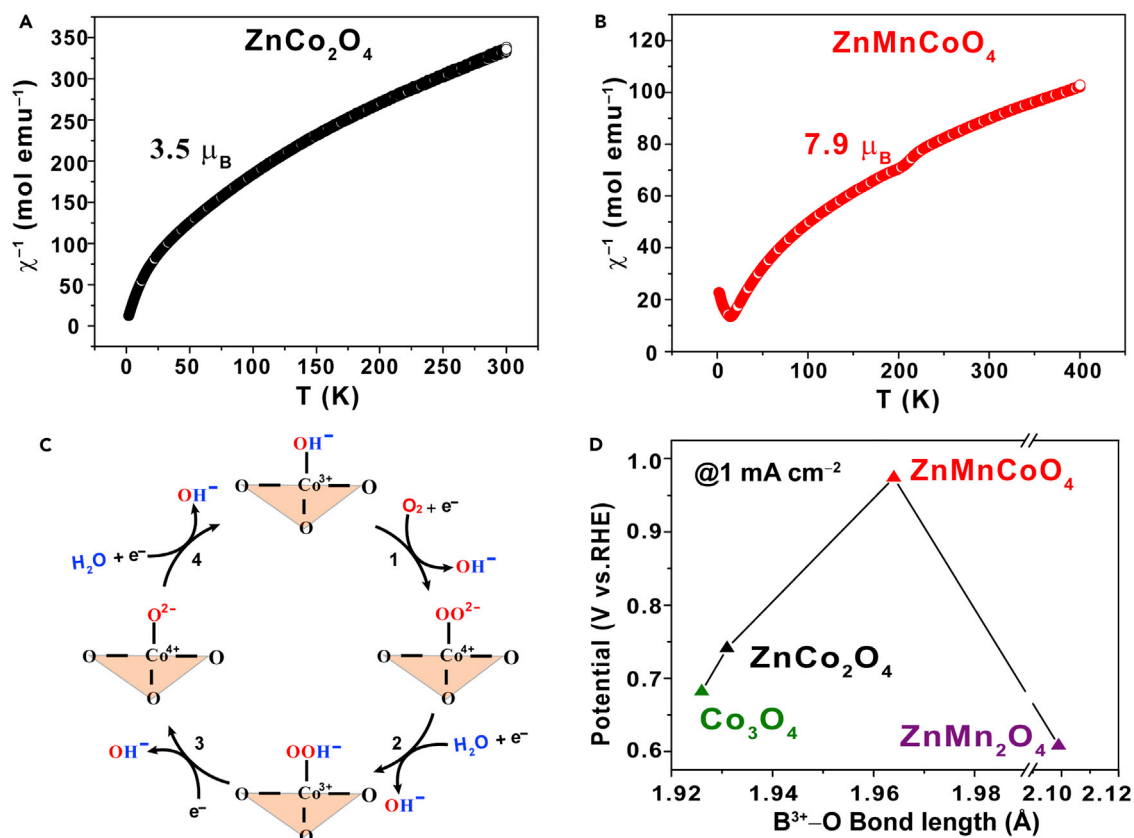


Figure 4. The Exploration of ORR Mechanism for $\text{ZnMn}_x\text{Co}_{2-x}\text{O}_4$

(A and B) Magnetic susceptibility of hollow porous (A) ZnCo_2O_4 and (B) ZnMnCoO_4 microspheres.

(C) The proposed ORR process occurring on the surface of Co^{3+} ions.

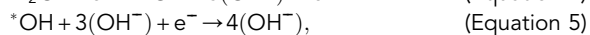
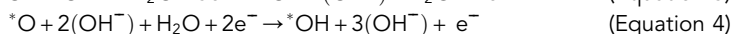
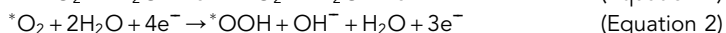
(D) The relationship between the ORR activity (i.e., onset potential) of a series of catalysts and the $\text{B}^{3+}\text{-O}$ bond length within the spinel oxide catalysts ($\text{B} = \text{Co}/\text{Mn}$).

weakened the $\text{Co}^{3+}\text{-O}$ bond and increased the bond length of $\text{Co}^{3+}\text{-O}$ bond from 1.926 Å in Co_3O_4 to 1.931 Å in ZnCo_2O_4 . Compared with Co_3O_4 , the Co^{3+} ions in ZnCo_2O_4 had a mixed low-spin and high-spin states because of the reduced $\text{Co}^{3+}\text{-O}$ covalent bond. On the other hand, Mn^{3+} ions with a larger size than Co^{3+} ions in the octahedral sites increased the lattice parameter of ZnMnCoO_4 and the bond length of $\text{Co}^{3+}\text{-O}$ to 1.964 Å. The effective magnetic moment of ZnMnCoO_4 ($7.9 \mu_{\text{B}}$ measured experimentally; Figure 4B) is close to the magnetic moment of ZnMnCoO_4 ($7.7 \mu_{\text{B}}$ theoretically calculated; $g = 2$) with high-spin states of Co^{3+} and Mn^{3+} ions, indicating that Co^{3+} ions in ZnMnCoO_4 had a higher ratio of high-spin states to low-spin states than Co^{3+} ions in ZnCo_2O_4 . The much more suitable population of highly energetic electrons in σ^* antibonding orbital of ZnMnCoO_4 than ZnCo_2O_4 destabilize the $\text{Co}^{3+}\text{-OH}^-$ bond and provide more energy to form a relatively stable $\text{Co}^{4+}\text{-O}_2^{2-}$ bond (step 1 in Figure 4C), thereby facilitating the $\text{O}_2^{2-}/\text{OH}^-$ displacement on the surface Co^{3+} ions of the spinel. Moreover, the rate of OH^- regeneration can be also improved due to the reduced $\text{Co}^{4+}\text{-O}_2^{2-}$ bond strength (step 4 in Figure 4C).

The relationship of catalytic activity of Co_3O_4 , ZnCo_2O_4 , ZnCoMnO_4 , and ZnMn_2O_4 catalysts and the bond length of $\text{Co}^{3+}\text{-O}$ is shown in Figure 4D. The ORR activity was greatly improved as the bond length of $\text{Co}^{3+}\text{-O}$ increased. In ZnMn_2O_4 catalyst, the

Mn³⁺ ion has a σ^* -antibonding-filling $e_g = 1$; however, Mn³⁺ with a strong Jahn-Teller effect and an Mn³⁺-O bond length of 2.099 Å (calculated from the XRD profile in Figure 2A) has a weak interaction with the oxygen and a low ORR activity. Moreover, recently Mn³⁺ ions in spinel LiNi_{0.5}Mn_{1.5}O₄ was found to be unstable in solution and underwent a disproportionation reaction to form Mn²⁺ and Mn⁴⁺ ions,²⁵ both of which have very low ORR activities. Thus, it is expected that the Mn³⁺ ions on the ZnMn₂O₄ catalyst surface may have low stability. Taken together, ZnMn₂O₄ catalyst exhibited a worse ORR performance.

The DFT calculations were then conducted to elucidate the relationship between the ORR activity and the spinel structure of crafted ZnMn_xCo_{2-x}O₄ catalysts. The ORR in alkaline solution proceeded via the following reactions.²⁶



where * represents the adsorbed species on the surface Co³⁺ ions. Alternatively, a peroxide intermediate OOH⁻ can be formed instead of the product in reaction (3) and desorbed from the catalytic site as a stable intermediate. The O²⁻/OH⁻ displacement on the surface Co³⁺ ions in reactions (1) and (5) are the rate-limiting steps of ORR in the alkaline solution.²⁷ The first step of ORR is the O₂ adsorption on the surface of catalyst (Figure 5A), the oxygen molecule and Co³⁺ ion on ZnCo₂O₄ surface forms a strong bond with a Co-O bond distance of 1.767 Å (second panel in Figure 5A). In sharp contrast, ZnMnCoO₄ has a larger Co-O bond distance of 1.820 Å (second panel in Figure 5B) and a weaker binding with O₂. Moreover, the oxygen molecule has an O-O bond distance of 1.448 Å in ZnMnCoO₄ (second panel in Figure 5B), which is much larger than that in ZnCo₂O₄ (1.312 Å; second panel in Figure 5A). As a result, the reaction (3) in ZnMnCoO₄ proceeds much faster and generates less peroxide intermediate OOH⁻ than that in ZnCo₂O₄. The dissociation of the oxygenated intermediated species such as *O and *OH in reactions (4) and (5) limits the ORR activity in spinel oxides. As shown in Figure 5, the Co-O bond lengths in ZnMnCoO₄ and ZnCo₂O₄ are 1.712 Å (third panel in Figure 5B) and 1.670 Å (third panel in Figure 5A), respectively, and the corresponding binding energy in ZnMnCoO₄ is smaller than that in ZnCo₂O₄. Consequently, ZnMnCoO₄ carries a more favorable binding energy with O₂ and oxygenated species (i.e., *O and *OH) over ZnCo₂O₄, thereby leading to the faster kinetics in the ORR process.

In summary, a set of hollow porous spinel ZnMn_xCo_{2-x}O₄ microspheres was successfully crafted by forming a metal ion/polymer coordination complex followed by calcination at elevated temperature. Subsequently, these were exploited as catalyst in ORR. Among all ZnB₂O₄ microspheres, ZnMnCoO₄ (x = 1) possessed a high onset potential of 1.00 V and an outstanding durability in the alkaline solution. An integrated experimental and theoretical study revealed that the 3d electrons in Co³⁺ ions transformed from low-spin states in Co₃O₄ (used as control) to a mixed high-spin and low-spin state in ZnCo₂O₄ and ZnMnCoO₄, which reduced the bond strength of Co³⁺-O²⁻ and increased the O²⁻/OH⁻ displacement. Compared with ZnCo₂O₄ catalyst, ZnMnCoO₄ catalyst was found to have a more favorable binding energy with O₂ and oxygenated species (i.e., *O and *OH), thus leading to the faster kinetics in ORR. As such, it may offer promising potential for use as an effective catalyst with high oxygen reduction activity and durability in fuel cells and metal-air batteries, among other applications.

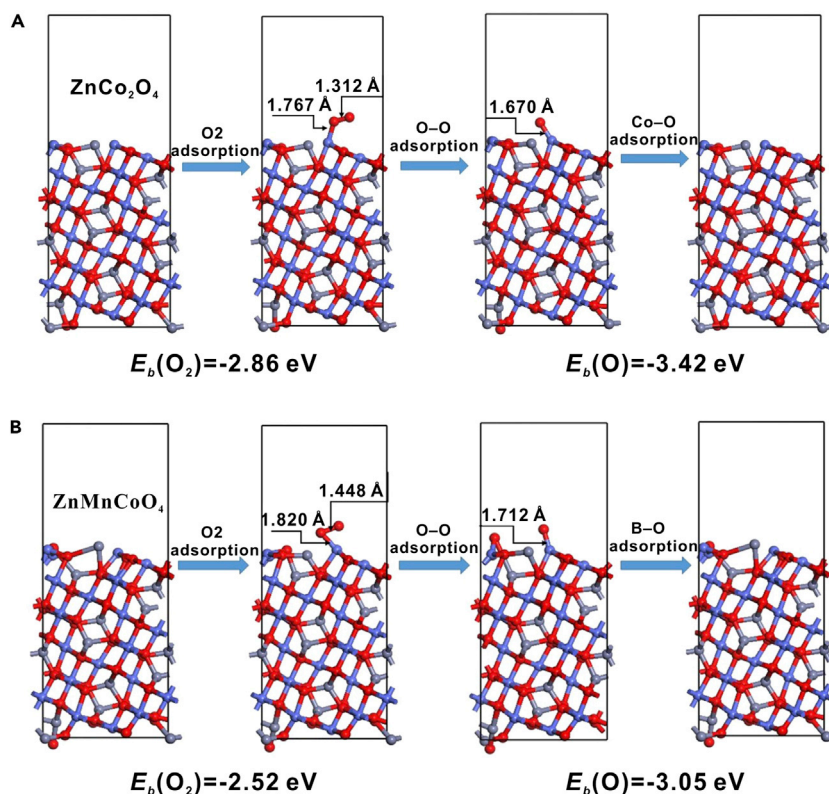


Figure 5. The DFT Calculations for Correlating the ORR Activity with the Spinel Structure of Crafted $\text{ZnMn}_x\text{Co}_{2-x}\text{O}_4$ Catalysts (i.e., ZnCo_2O_4 at $x = 0$ and ZnMnCoO_4 at $x = 1$)

(A and B) Optimized atomic structures for the main process of an ORR: (A) ZnCo_2O_4 and (B) ZnMnCoO_4 . The red circles and gray circles represent O atom and Zn atom, respectively. The blue circle refers to Co atom in (A) and represents B atom (i.e., 50% Mn and 50% Co atoms) in (B).

EXPERIMENTAL PROCEDURES

Synthesis of Hollow Porous $\text{ZnMn}_x\text{Co}_{2-x}\text{O}_4$ Microspheres

All hollow porous $\text{ZnMn}_x\text{Co}_{2-x}\text{O}_4$ ($0 \leq x \leq 2$) microspheres were synthesized by a two-step reaction. 0.3 g of polyvinyl pyrrolidone (PVP; molecular weight, $M_w = \sim 30,000 \text{ g/mol}$) was first dissolved in 150 mL of ethylene glycol to obtain a transparent solution. A stoichiometric amount of zinc acetylacetonate ($\text{Zn}(\text{C}_5\text{H}_7\text{O}_2)_2$), cobalt acetylacetonate ($\text{Co}(\text{C}_5\text{H}_7\text{O}_2)_3$), and manganese acetylacetonate ($\text{Mn}(\text{C}_5\text{H}_7\text{O}_2)_3$) (all in powder forms) were then added to the above solution at different cationic ratios under magnetic stirring at room temperature for 2 hr to yield desired $\text{ZnMn}_x\text{Co}_{2-x}\text{O}_4$ ($0 \leq x \leq 2$) microspheres. The mixture was then transferred to a flask and maintained at 190°C in an oil bath for 6 hr. The light-brown precipitate was collected by centrifugation and washed several times with ethanol. The as-synthesized precursors (i.e., the PVP and the metal ions coordinated complexes) were calcined at 500°C in air for 3 hr to yield the final product.

Commercial Co_3O_4 powder was also used as control without any further purification.

Characterization of Spinel Samples

Powder XRD was employed to monitor the phase formation over a 2θ range of 10° – 70° . High-resolution synchrotron XRD data was collected at Sector 11

ID-C beamline at the Advanced Photon Source, Argonne National Laboratory. A monochromatic X-ray beam with a wavelength of 0.1173 Å was used. The diffraction data were recorded by an amorphous silicon detector. The two-dimensional images were then integrated to one-dimensional patterns with the Fit2D program.

The morphology and microstructures of $\text{ZnMn}_x\text{Co}_{2-x}\text{O}_4$ samples were investigated by an S-4800 field-emission scanning electron microscope and a transmission electron microscope. The BET specific surface area of samples was analyzed by nitrogen adsorption with a V-Sorb 2800P Surface Area and Pore Distribution Analyzer.

The temperature dependence of magnetic susceptibility was conducted from 2 to 300 K under a magnetic field $H = 1$ T with a Superconducting Quantum Interference Device magnetometer.

Electrode Preparation and Electrochemical Measurement

All electrochemical measurements were carried out on an Autolab electrochemical workstation with a conventional three-electrode system in N_2 - and O_2 -saturated 0.1 M KOH solution. The Hg/HgO electrode, a Pt foil, and a glassy carbon electrode (GCE, 5 mm in diameter) were used as the reference, counter, and working electrodes, respectively. All the potential values were calibrated to reversible hydrogen electrode (RHE). The catalyst inks were prepared as follows: 5 mg of catalysts (including 1 mg of Vulcan XC-72 carbon black) and 20 μL of 5 wt.% Nafion were dispersed in 300 μL of deionized water and 700 μL of isopropanol. Ten microliters of catalyst ink with a catalyst loading of 0.25 mg cm^{-2} was dropped onto GCE and dried at room temperature. The cyclic voltammetry and LSV measurements were performed at a rate of 50 and 5 mV s^{-1} from 0.3 to 1.1 V (versus RHE), respectively. The chronoamperometric responses were conducted on a fixed potential of 0.6 V in an O_2 -saturated 0.1 M KOH solution; 3 M methanol was added into the electrolyte when the test proceeded to 500 s in the methanol tolerance experiment.

First-Principles Calculations

First-principles calculations were performed based on DFT with a plane-wave basis set for expansion of the wave functions that were implemented with the CASTEP program. CASTEP in Accelrys Materials Studio was used in this study. The geometrical structures and density of states were calculated with the PBE form for generalized gradient approximation (GGA). An energy cutoff of 500 eV and appropriate k point were chosen to ensure the convergence of total ground-state energy. The convergence in energy and force were 1×10^{-5} eV and 3×10^{-2} eV Å $^{-1}$, respectively. Since electron correlation with the d states significantly affects the electronic structure and energetic properties of transition metal oxides, the GGA + U approach was used to accurately calculate the O_2 binding energy with $U = 3.3$ eV. We only considered typical stoichiometric (311) surface, which exhibited the strongest signal in the XRD result. Inversion symmetrical slabs were used to remove the dipole moment. The inner two layers of the slab were frozen at bulk position to simulate the bulk of this material. The thicknesses of vacuum (10 Å), slab (~ 10 Å), and free relaxation layer were chosen to obtain a surface energy in the given direction converged to within 5% of the calculated value. The O_2 -binding and O-binding energies for the investigated catalysts were calculated as $E_b = E_{\text{substrate+adsorbate}} - E_{\text{substrate}} - E_{\text{adsorbate}}$, where E_b , $E_{\text{substrate+adsorbate}}$, $E_{\text{substrate}}$, and $E_{\text{adsorbate}}$ refer to the binding energy and the total

energy of the substrate and adsorbate, the substrate, and the adsorbate, respectively.²⁸

SUPPLEMENTAL INFORMATION

Supplemental Information includes nine figures and three tables and can be found with this article online at <https://doi.org/10.1016/j.joule.2017.11.016>.

ACKNOWLEDGMENTS

This work was financially supported by National Natural Science Foundation of China (nos. 61574020 and 61671085), Natural Science Foundation of Beijing (no. 2162037), Beijing Nova Program (no. Z171100001117077), and China Scholarship Council (no. 201606470040).

AUTHOR CONTRIBUTIONS

R.L., Y.L., M.L., and Z.L. conceived the idea and co-wrote the manuscript. M.L., Y.L., and Z.L. supervised the project. H.W., R.L., Y.L., Z.C., X. Lü, S.Z., Q.W., S.X., and K.Y. carried out the synthesis of materials and the electrochemical evaluation. Y.L., X. Li, S.X., and R.Z. helped with the materials characterization. All of the authors discussed the results and commented on the manuscript.

DECLARATION OF INTERESTS

The authors declare no competing interests.

Received: September 21, 2017

Revised: November 15, 2017

Accepted: November 29, 2017

Published: December 22, 2017

REFERENCES

1. Damour, C., Benne, M., Grondin-Perez, B., Bessafi, M., Hissel, D., and Chabriot, J.P. (2015). Polymer electrolyte membrane fuel cell fault diagnosis based on empirical mode decomposition. *J. Power Sources* *299*, 596–603.
2. de la Osa, A.R., Calcerrada, A.B., Valverde, J.L., Baranova, E.A., and de Lucas-Consuegra, A. (2015). Electrochemical reforming of alcohols on nanostructured platinum-tin catalyst-electrodes. *ACS Appl. Mater. Interfaces* *7*, 276–284.
3. Jia, Q., Ramaswamy, N., Hafiz, H., Tylus, U., Strickland, K., Wu, G., Barbiellini, B., Bansil, A., Holby, E.F., Zelenay, P., et al. (2015). Experimental observation of redox-induced Fe-N switching behavior as a determinant role for oxygen reduction activity. *ACS Nano* *9*, 12496–12505.
4. Kim, G., Eom, K., Kim, M., Yoo, S.J., Jang, J.H., Kim, H.J., and Cho, E. (2015). Design of an advanced membrane electrode assembly employing a double-layered cathode for a PEM fuel cell. *ACS Appl. Mater. Interfaces* *7*, 27581–27585.
5. Tang, H.J., Yin, H.J., Wang, J.Y., Yang, N.L., Wang, D., and Tang, Z.Y. (2013). Molecular architecture of cobalt porphyrin multilayers on reduced graphene oxide sheets for high-performance oxygen reduction reaction. *Angew. Chem. Int. Ed.* *52*, 5585–5589.
6. Fu, X.R., Hu, X.F., Yan, Z.H., Lei, K.X., Li, F.J., Cheng, F.Y., and Chen, J. (2016). Template-free synthesis of porous graphitic carbon nitride/carbon composite spheres for electrocatalytic oxygen reduction reaction. *Chem. Commun.* *52*, 1725–1728.
7. Zhu, J., He, G., Tian, Z., Liang, L., and Shen, P.K. (2016). Facile synthesis of boron and nitrogen-doped graphene sheets anchored platinum nanoparticles for oxygen reduction reaction. *Electrochim. Acta* *194*, 276–282.
8. Tang, H.J., Hessel, C.M., Wang, J.Y., Yang, N.L., Yu, R.B., Zhao, H.J., and Wang, D. (2014). Two-dimensional carbon leading to new photoconversion processes. *Chem. Soc. Rev.* *43*, 4281–4299.
9. Qi, J., Lai, X.Y., Wang, J.Y., Tang, H.J., Ren, H., Yang, Y., Jin, Q., Zhang, L.J., Yu, R.B., Ma, G.H., et al. (2015). Multi-shelled hollow micro-/nanostructures. *Chem. Soc. Rev.* *44*, 6749–6773.
10. Nam, G., Park, J., Choi, M., Oh, P., Park, S., Kim, M.G., Park, N., Cho, J., and Lee, J.S. (2015). Carbon-coated core-shell Fe-Cu nanoparticles as highly active and durable electrocatalysts for a Zn-Air battery. *ACS Nano* *9*, 6493–6501.
11. Wang, D., Xin, H.L., Hovden, R., Wang, H., Yu, Y., Muller, D.A., DiSalvo, F.J., and Abruña, H.D. (2013). Structurally ordered intermetallic platinum-cobalt core-shell nanoparticles with enhanced activity and stability as oxygen reduction electrocatalysts. *Nat. Mater.* *12*, 81–87.
12. Cui, X., Xiao, P., Wang, J., Zhou, M., Guo, W.L., Yang, Y., He, Y.J., Wang, Z.W., Yang, Y.K., Zhang, Y.H., and Lin, Z.Q. (2017). Highly branched metal alloy networks with superior activities for the methanol oxidation reaction. *Angew. Chem. Int. Ed.* *129*, 4559–4564.
13. He, B.C., Chen, X.X., Lu, J.M., Yao, S.D., Wei, J., Zhao, Q., Jing, D.S., Huang, X.N., and Wang, T. (2016). One-pot synthesized Co/Co₃O₄-N-graphene composite as electrocatalyst for oxygen reduction reaction and oxygen evolution reaction. *Electroanal.* *28*, 2435–2443.
14. Xu, X., Dai, Y., Yu, J., Hao, L., Duan, Y., Sun, Y., Zhang, Y., Lin, Y., and Zou, J. (2017). Metallic state FeS anchored (Fe)/Fe₃O₄/N-doped graphitic carbon with porous spongelike structure as durable catalysts for enhancing bioelectricity generation. *ACS Appl. Mater. Interfaces* *9*, 10777–10787.
15. Stephens, I.E., Bondarenko, A.S., Grønbjerg, U., Rossmeisl, J., and Chorkendorff, I. (2012). Understanding the electrocatalysis of oxygen

- reduction on platinum and its alloys. *Energ. Environ. Sci.* 5, 6744–6762.
- Suntivich, J., Gasteiger, H.A., Yabuuchi, N., Nakanishi, H., Goodenough, J.B., and Shao-Horn, Y. (2011). Design principles for oxygen-reduction activity on perovskite oxide catalysts for fuel cells and metal-air batteries. *Nat. Chem.* 3, 546–550.
 - Jung, J.-I., Risch, M., Park, S., Kim, M.G., Nam, G., Jeong, H.-Y., Shao-Horn, Y., and Cho, J. (2016). Optimizing nanoparticle perovskite for bifunctional oxygen electrocatalysis. *Energ. Environ. Sci.* 9, 176–183.
 - Kan, D., Orikasa, Y., Nitta, K., Tanida, H., Kurosaki, R., Nishimura, T., Sasaki, T., Guo, H., Ozaki, Y., and Uchimoto, Y. (2016). Overpotential-induced introduction of oxygen vacancy in $\text{La}_{0.67}\text{Sr}_{0.33}\text{MnO}_3$ surface and its impact on oxygen reduction reaction catalytic activity in alkaline solution. *J. Phys. Chem. C* 120, 6006–6010.
 - Aijaz, A., Masa, J., Rösler, C., Xia, W., Weide, P., Botz, A.J., Fischer, R.A., Schuhmann, W., and Muhler, M. (2016). $\text{Co}@\text{Co}_3\text{O}_4$ encapsulated in carbon nanotube-grafted nitrogen-doped carbon polyhedra as an advanced bifunctional oxygen electrode. *Angew. Chem. Int. Ed.* 55, 4087–4091.
 - Saitoh, T., Mizokawa, T., Fujimori, A., Abbate, M., Takeda, Y., and Takano, M. (1997). Electronic structure and temperature-induced paramagnetism in LaCoO_3 . *Phys. Rev. B* 55, 4257.
 - Zhang, G., Yu, L., Wu, H.B., Hoster, H.E., and Lou, X.W. (2012). Formation of ZnMn_2O_4 ball-in-ball hollow microspheres as a high-performance anode for lithium-ion batteries. *Adv. Mater.* 24, 4609–4613.
 - Tan, Y., Wu, C., Lin, H., Li, J., Chi, B., Pu, J., and Jian, L. (2014). Insight the effect of surface Co cations on the electrocatalytic oxygen evolution properties of cobaltite spinels. *Electrochim. Acta* 121, 183–187.
 - Yang, G., Xu, X., Yan, W., Yang, H., and Ding, S. (2014). Single-spinneret electrospinning fabrication of CoMn_2O_4 hollow nanofibers with excellent performance in lithium-ion batteries. *Electrochim. Acta* 137, 462–469.
 - Roth, W. (1964). The magnetic structure of Co_3O_4 . *J. Phys. Chem. Solids* 25, 1–10.
 - Xiao, J., Chen, X., Sushko, P.V., Sushko, M.L., Kovarik, L., Feng, J., Deng, Z., Zheng, J., Graff, G.L., and Nie, Z. (2012). High-performance $\text{LiNi}_{0.5}\text{Mn}_{1.5}\text{O}_4$ spinel controlled by Mn^{3+} concentration and site disorder. *Adv. Mater.* 24, 2109–2116.
 - Kattel, S., Atanassov, P., and Kiefer, B. (2012). Density functional theory study of $\text{Ni-N}_x/\text{C}$ electrocatalyst for oxygen reduction in alkaline and acidic media. *J. Phys. Chem. C* 116, 17378–17383.
 - Li, F., Shu, H., Hu, C., Shi, Z., Liu, X., Liang, P., and Chen, X. (2015). Atomic mechanism of electrocatalytically active Co-N complexes in graphene basal plane for oxygen reduction reaction. *ACS Appl. Mater. Interfaces* 7, 27405–27413.
 - Cheng, F., Shen, J., Peng, B., Pan, Y., Tao, Z., and Chen, J. (2011). Rapid room-temperature synthesis of nanocrystalline spinels as oxygen reduction and evolution electrocatalysts. *Nat. Chem.* 3, 79–84.